Band bending and alignment at the spinel/perovskite γ-Al$_2$O$_3$/SrTiO$_3$ heterointerface

P. Schütz,[1] F. Pfaff,[1] P. Scheiderer,[1] Y. Z. Chen,[2] N. Pryds,[2] M. Gorgoi,[3] M. Sing,[1] and R. Claessen[1]

[1]*Physikalisches Institut and Röntgen Center for Complex Material Systems (RCCM), Universität Würzburg,*
Am Hubland, 97074 Würzburg, Germany

[2]*Department of Energy Conversion and Storage, Technical University of Denmark, Risø Campus, 4000 Roskilde, Denmark*

[3]*Helmholtz-Zentrum für Materialien und Energie GmbH, 12489 Berlin, Germany*

We present a comprehensive study of the band bending and alignment at the interface of γ-Al$_2$O$_3$/SrTiO$_3$ heterostructures by hard x-ray photoelectron spectroscopy. Our measurements find no signs for a potential gradient within the polar γ-Al$_2$O$_3$ film as predicted by the basic electronic reconstruction scenario. We present evidence for a band bending on the SrTiO$_3$ side of the interface, yielding a roughly 600 meV deep potential trough, which reaches below the chemical potential and has a spatial expansion of 3–5 unit cells. The band offset between the bulk valence bands is determined to be also approximately 600 meV, corresponding to aligned bands at the interface. Finally, the spatial confinement of the interfacial two-dimensional electron system is derived from the chemically shifted Ti^{3+} photoemission signal in the Ti 2p core level spectra, measured at various photoelectron detection angles. It is found to be in excellent agreement with the spatial depth of the potential trough.

I. INTRODUCTION

Breaking the translation or inversion symmetry at the interface of oxide heterostructures may lead to unexpected and novel phenomena, a prominent example being the formation of a two-dimensional electron system (2DES) at the interface between TiO$_2$-terminated SrTiO$_3$ (STO) and a heteroepitaxial LaAlO$_3$ (LAO) thin film at and above a critical overlayer thickness of four unit cells (uc) [1,2]. While oxygen defects [3] or cation intermixing [4,5] have been suggested as possible origin of the 2DES, the most discussed explanation is electronic reconstruction driven by the polar discontinuity between the nonpolar STO and the polar LAO overlayer [6]. In this scenario, the built-in potential within the LAO film is compensated by a transfer of electrons from the surface to the interface, where according to density-functional theory a potential trough forms as the STO conduction band minimum (CBM) bends below the chemical potential [7–10]. The otherwise empty Ti 3d-derived quantum well states become populated by the electronic reconstruction mechanism and form the 2DES with a width of only a few unit cells [11,12].

Recently, a new type of 2DES at the interface between perovskite STO and a heteroepitaxial spinel γ-Al$_2$O$_3$ (GAO) thin film has been reported [13,14]. Electron mobilities exceeding those hitherto observed in all-perovskite heterostructures by more than one order of magnitude are obtained, thus showing promise for future applications in all-oxide devices or mesoscopic physics with strongly correlated electrons. Similar to LAO/STO, a critical thickness behavior for interface conductivity is found in GAO/STO heterostructures, which also exhibit a polar discontinuity at the interface between the nonpolar STO and the polar GAO overlayer. Accordingly, one would expect the existence of a potential gradient within the overlayer, as well as a potential trough on the STO side of the interface.

Hard x-ray photoelectron spectroscopy (HAXPES) is a suitable tool to investigate the electronic properties of oxide heterostructures due to its high probing depth and interface sensitivity. It provides detailed information of both the film

and the substrate [12] and is in principle capable of detecting a built-in potential, as shown for other polar oxide heterostructures [15]. In this paper, we present a comprehensive analysis of the band arrangement at the GAO/STO heterointerface as inferred from HAXPES measurements. Based on a detailed analysis of core-level spectra, we address the questions of a band bending within the GAO thin film as well as the STO substrate. Moreover, the band alignment between GAO and STO is deduced independently from core level and valence band spectra. Finally, an estimate for the spatial electron confinement at the interface is obtained from Ti core level spectra.

II. EXPERIMENT

The HAXPES experiment was performed at the crystal monochromator beamline KMC-1 of the third-generation storage ring BESSY II, Berlin, using the HIKE end station [16,17]. Spectra were taken at a photon energy of 3 keV with a total energy resolution of $\Delta E \approx 500$ meV. Binding energies were calibrated with reference to the Au Fermi edge and/or Au 4f core level at 84.0 eV.

GAO/STO samples with conducting interfaces (overlayer thicknesses 1.5, 2.0, 2.5, 3.0, and 22 uc) were prepared by pulsed laser deposition (PLD) as described elsewhere [13]. Film growth was monitored by reflection high-energy electron diffraction (RHEED). The oxygen partial pressure and substrate temperature were set to 1×10^{-4} mbar and 600 °C, respectively. All samples were contacted with conductive silver paint to ensure good electrical contact between the interfacial 2DES and the sample holder to prevent charging during photoemission.

All heterostructures were measured at different emission angles $\theta = 10°, \ldots, 50°$ with respect to the surface normal. By going to larger emission angles, the effective electron escape length decreases as $\lambda_{\text{eff}} = \lambda \cos \theta$, thereby increasing interface sensitivity. As reference samples for bulk STO and GAO spectra, we used a bare Nb-doped STO substrate (0.5 wt.%) and a thick GAO film (22 uc, approximately 18 nm),

respectively. The former was measured at $\theta = 10°$ to increase bulk sensitivity, whereas the latter was measured at $\theta = 40°$ to eliminate any signal from the substrate. All samples were transported in an desiccator and were measured at room temperature without further surface preparation.

III. RESULTS

A. Polar discontinuity at the interface and potential gradient in γ-Al$_2$O$_3$

While Al$_2$O$_3$ is a widely used oxide with a thermodynamically stable α phase of the corundum type, nanoscale synthesis can result in the formation of the spinel γ phase due to its lower surface energy [18]. The cubic spinel unit cell with stoichiometry AB$_2$O$_4$ is made up of 32 oxygen anions in a cubic close-packed arrangement and 24 cations, of which the 16 B cations are placed in octahedral and the 8 A cations in tetrahedral interstices [Fig. 1(a)].

As is the case for the perovskite structure, in the ionic limit the spinel structure can be interpreted as stacking of atomic layers. The unit cell consists of eight layers, alternately occupied by either octahedral or tetrahedral cations, as depicted in Fig. 1 (b). Due to the absence of oxygen anions in tetrahedral layers, they are not charge neutral. According to the classification by Tasker [19], like LAO, GAO is a polar type 3 crystal with nonvanishing electric dipole moment in [001] direction.

Since the polar discontinuity at the LAO/STO interface is deemed to play an important role in the emergence of the conducting interface, the question arises whether the strength of polarity in γ-Al$_2$O$_3$ is comparable. Here, Al ions adopt the A and B cation sites of the spinel structure. Writing the stoichiometry in standard spinel notation, Al$_{3-\delta}$O$_4$ with $\delta = \frac{1}{3}$, reveals that GAO adopts a defect-spinel structure [20]. Whether these cation vacancies preferably adopt one of the cation sites has been discussed controversially [20–22] and strongly affects the potential buildup inside the material. From simple electrostatics, taking into account layer spacings and neglecting all other material properties (e.g., the dielectric constant), one obtains the same nominal potential buildup as in LAO for cation vacancies exclusively in tetrahedral sites.

For vacancies only in octahedral cation sites a 1.5 times larger potential buildup is expected.

A built-in polar field and thus the presence of a potential gradient would have several consequences, which are in principle spectroscopically observable by HAXPES [15]. First, the O $2p$-derived film valence band states will be pushed towards (and above) the chemical potential. Thus, spectral weight should be observable at and below the chemical potential due to the occupied states in the GAO layer. Second, all atomic film core levels will track the potential slope, resulting in asymmetrically broadened and shifted spectra. Furthermore, the built-in field is reduced for film thicknesses larger than the critical thickness due to charge transfer from the surface towards the interface. A distinct film thickness dependence is thus expected for the film core level peak shapes, caused by the reduced relative energy shift per film layer [23].

Figure 2(a) shows the valence band spectrum of a 2.5 uc GAO/STO heterostructure. The valence band maximum (VBM) is determined from the intersection of a linear fit of the valence band edge with the zero-intensity baseline to lie at ≈ 3.5 eV [24]. No spectral O $2p$ valence band weight is found in the gap or at the chemical potential, thus indicating the absence of a potential gradient within the GAO film. The absence of spectral weight from interfacial Ti $3d$ charge carriers is due to the very small Ti $3d$ photoionization cross section for hard x rays [25,26].

Additionally, Al core level spectra were measured for all heterostructures. Figure 2(b) shows the Al $1s$ spectra of four heterostructures with different GAO thicknesses measured at an emission angle $\theta = 50°$. The spectral shape is identical for all samples, as observed for all film core levels. Furthermore, in Fig. 2(c) emission angle-dependent measurements, varying the probing depth from approximately 45–30 Å, show no sign of any asymmetry or spectral change, thus evidencing the flat-band behavior inside the film.

All spectroscopic findings are at variance with the sizable potential gradient in the film expected from the standard electronic reconstruction scenario. Similar observations have been made for other polar oxide heterostructures. In particular, the related heterostructure LAO/STO does not show a potential gradient as inferred from HAXPES [5,23,27–30].

B. Band bending in SrTiO$_3$

The influence of a potential bending inside the STO substrate in vicinity of the interface has been studied intensively by theory. For LAO/STO at and beyond the critical thickness, density-functional theory (DFT) calculations predict a bending of the conduction band minimum of more than 500 meV, thus forming a potential trough reaching below the chemical potential within the first five STO layers ($T = 0$ K) [7,9,31]. The resulting Ti $3d$-derived quantum-well states become populated and form the narrow interfacial 2DES [6,12,32].

An experimental verification of the band bending is possible by means of HAXPES, since the binding energies of all substrate core levels as a function of depth z below the interface trace the potential bending, thus leading to asymmetric line shapes as depicted in Fig. 3. The line shape of a given core level peak results from a superposition of the energy-shifted spectra of atoms within the bending zone [following the bent
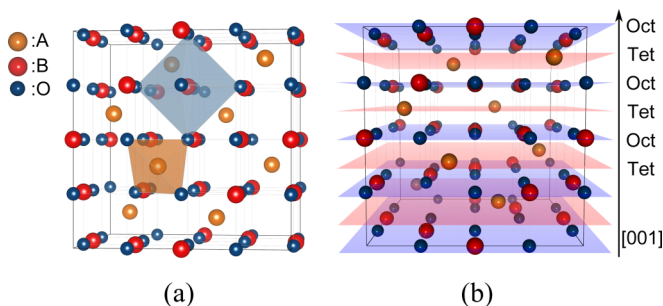

FIG. 1. (Color online) (a) The cubic spinel unit cell contains 32 oxygen atoms in cubic close-packed arrangement. The 8 A cations are located in tetrahedral (yellow) and the 16 B cations in octahedral interstices (blue). (b) In the [001] direction, the crystal structure can be considered as stacking sequence of octahedral and tetrahedral layers. Note that γ-Al$_2$O$_3$ exhibits cation vacancies and thus adopts a defect-spinel structure.
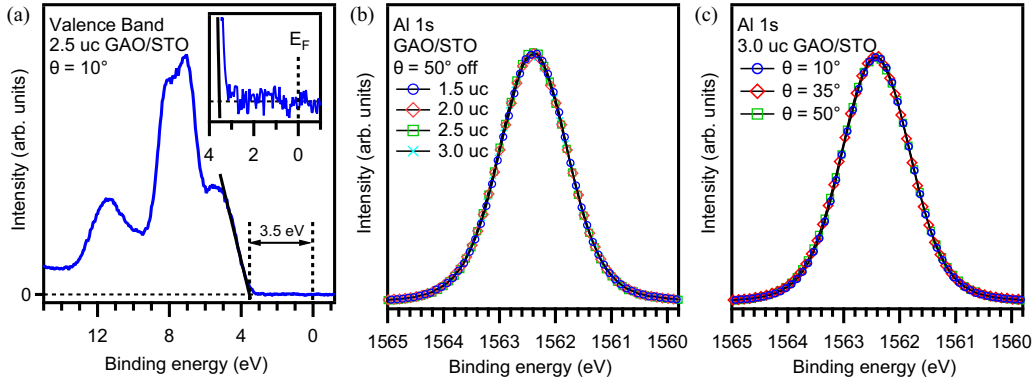
FIG. 2. (Color online) (a) Valence band spectrum of a 2.5 uc GAO/STO heterostructure. No spectral weight is found in the band gap, signaling the absence of a potential gradient. The valence band maximum (VBM) is determined from the intersection of a linear fit of the leading edge and the constant background. (b) Al 1*s* core level spectra of four GAO/STO heterostructures with varying GAO thickness. No change in spectral shape is observed. Spectra are normalized to same integrated peak area. (c) Al 1*s* core level emission angle-dependence of a 3.0 uc GAO/STO heterostructure. No asymmetry or deviation in the spectral shape is found.

potential $E_{bb}(z)$] and the contribution of atoms in the bulk (at fixed binding energy). The relative intensities of all superposed core level spectra are determined by a Beer-Lambert law. A variation of the emission angle θ alters the effective probing depth and thus the ratio of the photoemission signals from bending zone and unaffected bulk, which manifests itself in a varying degree of asymmetry.

To receive as accurate results as possible, a refined background correction taking into account the complex electron

FIG. 3. (Color online) Illustration of the effect of band bending in STO on the Sr 3*d* line shape. The emission from each SrO layer is damped by an exponential damping factor (Beer-Lambert law) and shifted in energy according to the bent potential $E_{bb}(z)$. The resulting line shape is a superposition of a number of spectra from the bending zone and the sum of all remaining core level spectra at the bulk binding energy. The GAO overlayer only accounts for an overall damping factor, which does not affect the line shape.

energy loss spectrum of STO [33] was performed to obtain the intrinsic spectra (for details see Supplemental Material [34]). The resulting emission angle-dependent Sr 3*d* and Ti 2$p_{3/2}$ spectra of a 3.0 uc GAO/STO sample are shown in Fig. 4 (bottom). All spectra are normalized to same integrated peak area and systematically show a growing asymmetry towards higher binding energy with increasing emission angle θ. The Ti 2$p_{3/2}$ core level spectra further exhibit a slight shoulder at lower binding energy [see Fig. 4(b), inset], which is assigned to the chemically shifted photoemission from Ti^{3+} ions at the interface and will be matter of discussion in Sec. III D. Note that the Ti 2$p_{1/2}$ core level is not suitable for an analysis since it always shows an asymmetry due to multiplet splitting. Additionally, Fig. 4 (top) shows difference spectra of the respective core levels, where an emission angle of 10° corresponding to maximum bulk sensitivity is chosen as reference spectrum. The sizable and systematic effect of the asymmetric broadening due to band bending at the interface is highlighted.

For a more quantitative analysis, a simple model is introduced. The emission from core levels is assumed to be localized at the respective cation sites in ideal stoichiometric samples with bulk lattice constant a. Taking into account the exponential damping of the photoelectron signal, the layer-dependent emission intensity can be described as $I(z = na) = I_0 \exp(-a/\lambda_{\text{eff}})^n$, where n indicates the emitting layer and I_0 is the undamped emission intensity per layer. Note that I_0 can be considered constant for all layers, since the x-ray penetration depth exceeds the photoelectron attenuation length by approximately two orders of magnitude [35]. The ratio between bulk and bending zone intensity is determined by the effective inelastic mean-free path $\lambda_{\text{eff}} = \lambda_{\text{IMFP}} \cos \theta$, which implicitly includes the angle of emission θ and the inelastic mean-free path λ_{IMFP}. While θ is known from experiment, λ_{IMFP} is obtained from the TPP2 relation applied to STO [36]. Note that the γ-Al$_2$O$_3$ overlayer only leads to an overall damping of the entire signal and hence does not influence the line shape.

In light of the only subtle effects in the asymmetric core level spectra, a phenomenological model for the bent potential
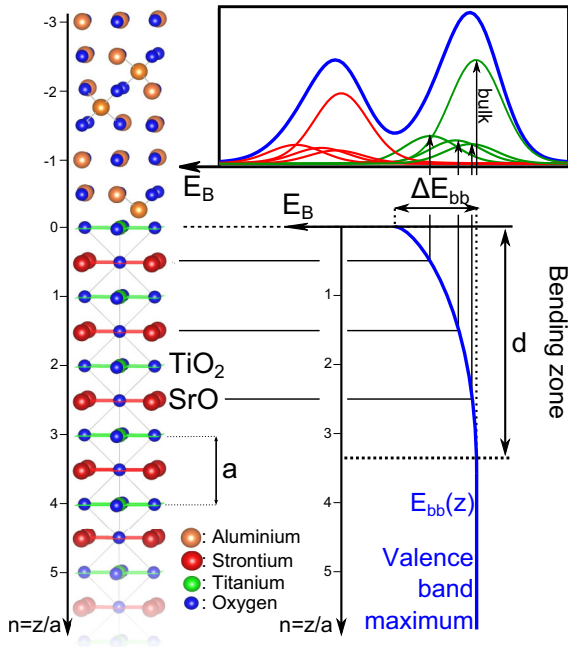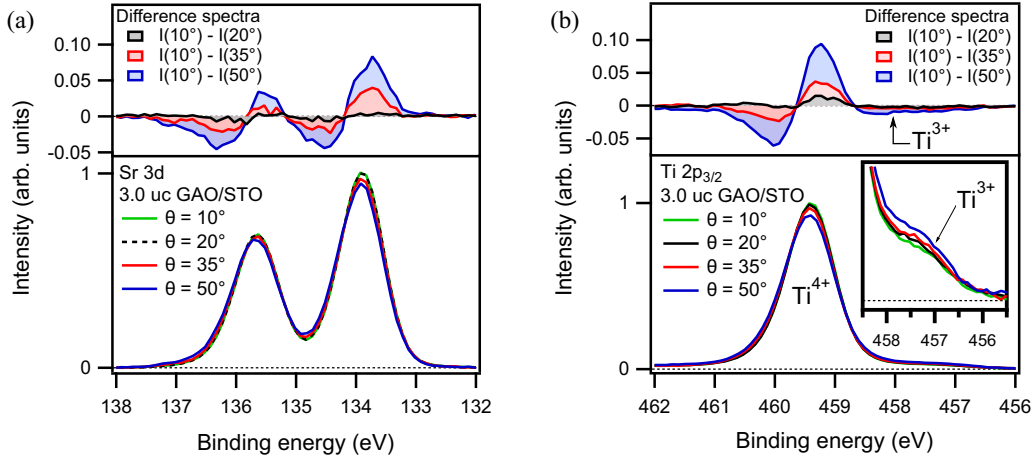
FIG. 4. (Color online) (a) Sr $3d$ and (b) Ti $2p_{3/2}$ core level spectra of a 3.0 uc GAO/STO heterostructure. Bottom: Angle-dependent background-corrected substrate core level spectra. Top: Difference spectra as indicated. All spectra show a systematic asymmetric broadening towards higher binding energy with increasing emission angle, corresponding to higher interface sensitivity. The difference spectra corroborate and distinguish the systematic behavior. Inset in (b): Shoulder at the lower binding energy side, due to photoemission from the chemically-shifted 3+ state of interfacial Ti ions with an extra $3d$ electron.

$E_{bb}(z)$ is introduced instead of a more thorough treatment involving a self-consistent solution of the Poisson-Schrödinger equation. As approximation, a bent potential of the form $E_{bb}(z) = \Delta E_{bb}(\frac{z}{d} - 1)^2$ for $0 < z < d$ and 0 elsewhere is used, which is parametrized by its depth ΔE_{bb} and spatial expansion d as depicted in Fig. 3. Each atomic layer n is assumed to emit an identical symmetric Voigt spectrum, shifted by $E_{bb}(z = na)$ and damped according to $I(z = na)$.

Since the band-bending effects are subtle, no reliable values for ΔE_{bb} and d can be deduced from the analysis of single spectra. For this reason, a global fitting scheme is employed to consistently and simultaneously fit all measured spectra, i.e., the Sr $3d$ and Ti $2p_{3/2}$ spectra for four GAO film thicknesses (1.5, 2.0, 2.5, 3.0 uc) and four emission angles ($10°$, $20°$, $35°$, $50°$), amounting to 48 fit peaks (and 288 independent parameters) in total. In physically reasonable cases constraints are introduced to specific parameters, which set them as equal

for all/some spectra, e.g., the Gaussian and Lorentzian full width at half maximum (FWHM) for each core level or ΔE_{bb} and d for one and the same sample, thus reducing the number of independent parameters to 47 (approximately one per measured spectrum). Due to the consistency in the global fitting scheme, well-founded conclusions can be drawn about the band bending.

Exemplary fitting results for the Sr $3d$ and Ti $2p_{3/2}$ spectra of a 3.0 uc GAO/STO heterostructure are shown in Fig. 5 and Fig. 6, respectively. The panels in Figs. 5(a) and 6(a) show fit results and residual curves for three values of θ. The increasing interface sensitivity for increasing θ manifests itself in the changing relative intensities from bending zone and bulk, as highlighted by horizontal dashed lines as guide to the eye. Figures 5(b) and 6(b) summarize the fit results (bottom panel) and give a comparison between difference spectra of experimental and fit curves (top panel). Obviously, the model
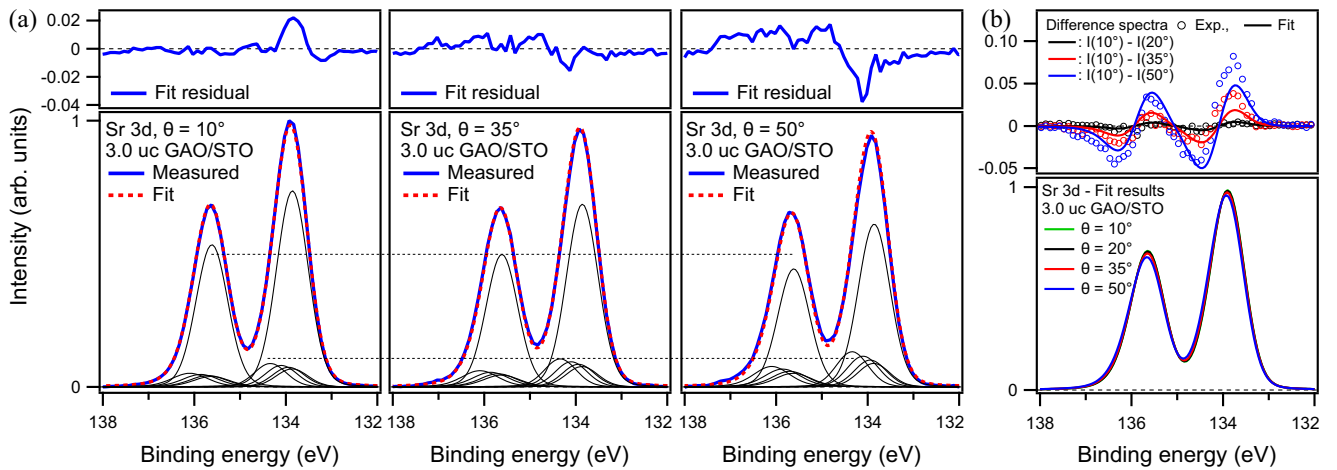

FIG. 5. (Color online) (a) Exemplary fit results and residuals for the Sr $3d$ core level of a 3.0 uc GAO/STO heterostructure. The changing relative intensity between bending zone and bulk signal reflects the increasing interface sensitivity with increasing angle of emission θ. (b) Bottom: Fit results for all emission angles. Top: Comparison between difference spectra of experimental and fit curves. For details see text.
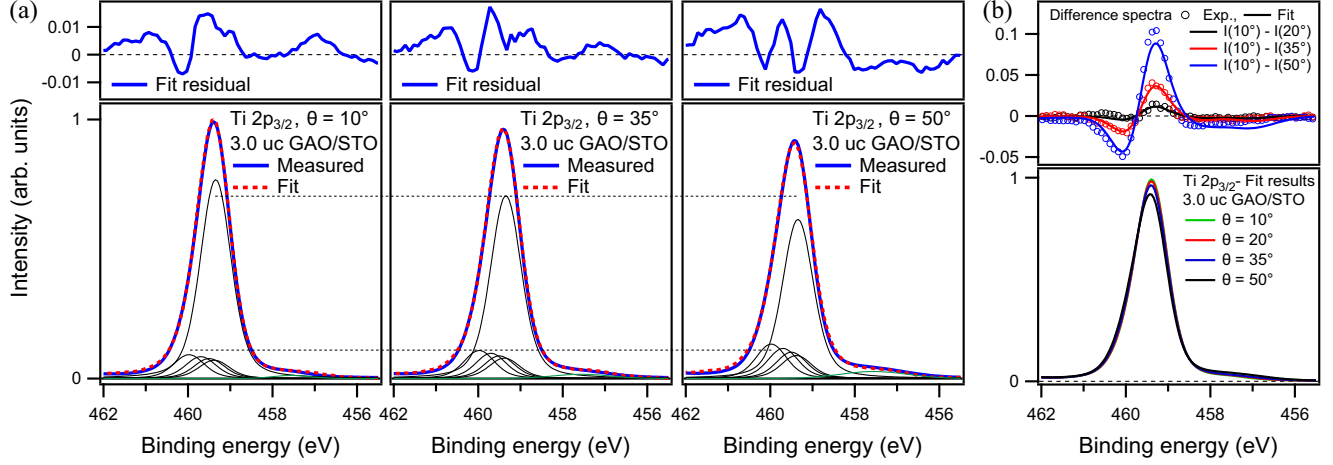
FIG. 6. (Color online) (a) Exemplary fit results and residuals for the Ti $2p_{3/2}$ core level of a 3.0 uc GAO/STO heterostructure. The changing relative intensity between bending zone and bulk signal (dashed lines) reflects the increasing interface sensitivity with increasing angle of emission θ. (b) Bottom: Fit results for all emission angles. Top: Comparison between difference spectra of experimental and fit curves.

consistently reproduces the observed systematic trend. While small deviations are due to the simplified assumption of a parabolic potential, the exact functional shape of the potential does not influence our results within experimental accuracy.

The results of the quantitative analysis are shown in Table I. The spatial expansion of the bending zone into the substrate d amounts to approximately 1.5 nm, corresponding to 3–5 unit cells of STO, and is essentially independent of the GAO overlayer thickness. The potential trough depth ΔE_{bb} is of the order of 600 meV and shows a decreasing trend towards the critical thickness $d_c = 1.5$ uc. While also discernible in the raw data, this trend is only feeble and at the resolution limit of this approach, which is reflected in the estimated experimental uncertainty of 150 meV.

C. Band alignment at the interface

Due to its sensitivity to both the film and the substrate, HAXPES is a suitable tool to determine the relative alignment of the valence band maxima (VBM) on both sides of the interface, i.e., the valence band offset ΔE_{VB}. Experimentally, two independent methods are available, the first of which is based on a decomposition of the heterostructure valence band spectrum into its contributions from substrate and overlayer. For this purpose, the measured spectrum is fit by a superposition of the GAO and STO bulk valence bands, with the relative energetic shift and intensity as fitting parameters to be determined.

Figures 7(a) and 7(b) show bulk reference spectra measured on a thick GAO film (22 uc) and a Nb-doped STO substrate. The respective valence band maximum (VBM) is determined from the intersection of a linear extrapolation of the leading edge and the constant background (gray dashed lines) [24,37]. While both reference samples show a large band gap, the VBM of GAO lies significantly further below the chemical potential [VBM$_{\mathrm{GAO}} = (4.7 \pm 0.1)$ eV and VBM$_{\mathrm{STO}} = (3.5 \pm 0.1)$ eV]. Figure 7(c) shows the decomposition of the valence band of a 2.5 uc GAO/STO heterostructure. The valence band clearly exhibits two features unambiguously related to substrate and overlayer. The resulting superposition shows excellent agreement with the measured spectrum. Note that, while having only minor effects on the results for ΔE_{VB}, the band bending determined in the previous section is included. The total photoemission signal from STO (thick green line) consists of a signal from the bulk (thin green) and the bending zone

TABLE I. Results of the band-bending and band-alignment analysis. For details see text.

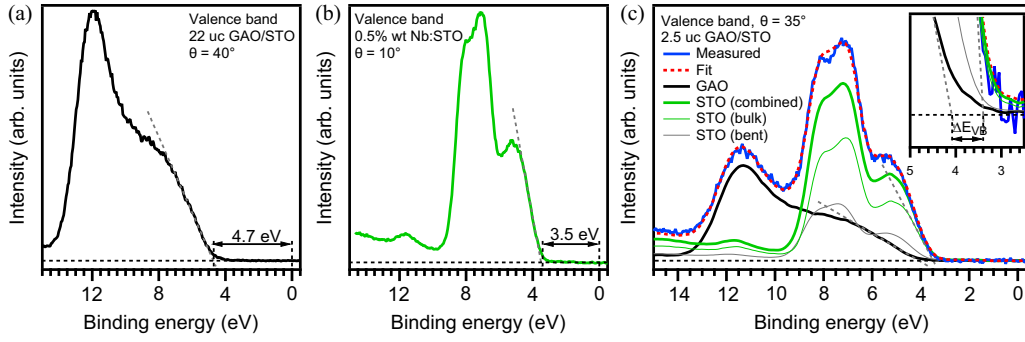| Film thickness (uc)	Nb:STO	1.5	2.0	2.5	3.0	22
			Band-bending analysis			
ΔE_{bb} (± 0.15 eV)	–	0.52	0.57	0.61	0.63	–
d (± 0.3 nm)	–	1.5	1.6	1.6	1.5	–
			Band-alignment analysis			
E_{VBM} (± 0.1 eV)	3.5	–	3.5	3.5	–	4.7
$E_{\mathrm{Sr}\,3d_{5/2}}$ (± 0.1 eV)	133.4	–	–	–	–	–
$E_{\mathrm{Al}\,2s}$ (± 0.1 eV)	–	–	–	–	–	120.2
$E_{\mathrm{Sr}\,3d_{5/2}} - E_{\mathrm{Al}\,2s}$ (± 0.05 eV)	–	13.88	13.77	13.73	13.70	–
ΔE_{VB} (± 0.15 eV) (CL analysis)	–	0.52	0.62	0.67	0.70	–
ΔE_{VB} (± 0.15 eV) (VB analysis)	–	–	0.60	0.62	–	–
ΔE_{CB} (± 0.15 eV)	–	3.88	3.79	3.76	3.70	–

FIG. 7. (Color online) (a) Valence band spectrum of a thick GAO film (22 uc), measured at an emission angle $\theta = 40°$. Gray dashed curves indicate the linear extrapolation of the valence band leading edge used for the determination of the valence band maximum (VBM). (b) Valence band spectrum of a Nb-doped STO substrate, measured at $\theta = 10°$. (c) Analysis of the valence band of a 2.5 uc GAO/STO heterostructure. The fit spectral shape (red dashed) shows excellent agreement with the measured spectrum (blue). Band bending results are included. The total signal from the STO substrate (thick green) is composed of the bulk contribution (thin green) and the emission from the bending zone (thin gray). Inset: Determination of the valence band offset ΔE_{VB} by linear extrapolation of the leading edge of each (bulk) reference contribution.

(thin gray). A detailed view of the determination of the valence band offset ΔE_{VB} by linear extrapolation of the leading edges is provided in the inset of Fig. 7(c), while the results are shown in Table I.

Alternatively, the valence band offset ΔE_{VB} can be determined from a core level analysis. For each reference sample the energy separation of a core level with respect to the VBM needs to be measured. In the heterostructure, the valence bands align with a certain offset. However, the energy separation of core levels with respect to the VBM ($\Delta E_{STO/GAO}$) does not change to a good approximation. Accordingly, the band offset can be derived from the energy separation of two core levels, one specific for the substrate and one for the film [38,39]. Including the band gaps Δ of GAO and STO, also the conduction band offset ΔE_{CB} is attainable:

$$\Delta E_{VB} = \left(E_{Sr3d_{5/2}} - E_{VBM} \right)_{STO} - \left(E_{Al2s} - E_{VBM} \right)_{GAO}$$
$$- \left(E_{Sr3d_{5/2}} - E_{Al2s} \right)_{GAO/STO} \tag{1}$$

$$\Delta E_{CB} = \Delta_{GAO} - \Delta_{STO} - \Delta E_{VB}. \tag{2}$$

The Sr $3d_{5/2}$ and Al $2s$ spectra are used for the core level analysis. Since the peak position of the Sr $3d_{5/2}$ spectrum is slightly affected by the band bending in the heterostructure, we use as bulk binding energy the value extracted from the band bending analysis in Sec. III B. The used experimental data values and the calculated values for the valence band offset ΔE_{VB} are summarized in Table I. Core level and valence band analysis yield consistent results for the valence band offset. The valence band offset ΔE_{VB} is of similar magnitude as the maximum band bending ΔE_{bb} (≈ 600 meV) and exhibits a similar decreasing trend towards the critical GAO overlayer thickness. Furthermore, the positive sign of ΔE_{VB} means that the VBM of STO is above that of GAO, corresponding to an interface of type I. This distinguishes GAO/STO from the case of LAO/STO, where the interface is found to be of type II [5,28,30,40].

D. Interfacial confinement of charge carriers

The conduction band of STO mainly arises from Ti $3d$ t_{2g} states, which become occupied in the potential trough

at the GAO/STO interface. Since the direct investigation of the interfacial 2DES by HAXPES is hindered by the small photoabsorption cross section of Ti $3d$ states, an indirect analysis based upon Ti $2p$ core levels, which exhibit a three orders of magnitude higher cross section [25,26], is the method of choice. As shown in Ref. [13] by conventional x-ray photoemission spectroscopy, an additional electron in the Ti $3d$ shell leads to a valence shift from Ti^{4+} to Ti^{3+}, which manifests itself in a chemical shift towards lower binding energies in the Ti $2p$ core level photoemission. Figure 8(a) shows Ti $2p_{3/2}$ spectra of the Nb-doped STO reference and a 2.0 uc GAO/STO sample. At higher binding energies the band bending causes an asymmetric broadening, while the chemically shifted Ti^{3+} spectral weight is seen at the lower binding energy side (see inset) [12].

The narrow confinement of the Ti $3d$ states is signaled by the angle dependence of the Ti^{3+}/Ti^{4+} intensity ratio, as, e.g., shown in Fig. 4(b), inset. For a more quantitative analysis, a simple model is used [12]. The 2DES is assumed to extend into the substrate to a depth d_{2DES}. The Ti $3d$ electrons are homogeneously distributed in this region with a fraction p of Ti^{3+} ions. Taking into account the exponential damping, the ratio of Ti^{3+} to Ti^{4+} signal as function of emission angle
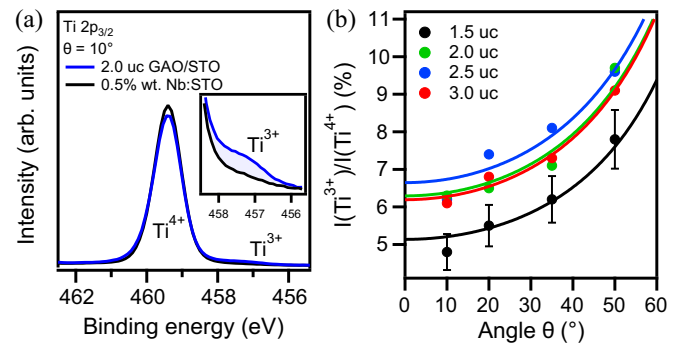

FIG. 8. (Color online) (a) Ti $2p_{3/2}$ spectrum of bare Nb:STO and a GAO/STO heterostructure. The bare Nb:STO shows neither a band bending asymmetry nor chemically shifted Ti^{3+} emission. (b) Ti^{3+} to Ti^{4+} intensity ratio as function of emission angle.

TABLE II. Results of the Ti^{3+} $2p$ analysis. A slightly enhanced two-dimensional charge carrier concentration is found for the 2.5 uc GAO/STO sample. For details see text and Supplemental Material.

	1.5 uc	2.0 uc	2.5 uc	3.0 uc
d_{2DES} (Å)	5...15	6...21	7...23	6...21
p	0.15...0.4	0.15...0.4	0.15...0.4	0.15...0.4
n_{2D} (10^{14} cm^{-2})	3.7 ± 0.4	4.7 ± 0.6	5.2 ± 0.5	4.6 ± 0.6

becomes

$$\frac{I(\text{Ti}^{3+})}{I(\text{Ti}^{4+})}(\theta) = \frac{p\left[1 - \exp\left(-\frac{d_{2DES}}{\lambda_{IMFP}\cos(\theta)}\right)\right]}{1 - p\left[1 - \exp\left(-\frac{d_{2DES}}{\lambda_{IMFP}\cos(\theta)}\right)\right]}. \quad (3)$$

The ratio is determined from an analysis of the Ti $2p_{3/2}$ spectra, as shown exemplarily in Fig. 6. The resulting data points together with fit curves according to Eq. (3) for all samples are shown in Fig. 8(b). Error bars representing an experimental uncertainty of ±10% are shown for one curve. Considerably less Ti^{3+} spectral weight is found for the 1.5 uc GAO/STO sample in comparison to the other samples. Furthermore, a slightly enhanced Ti^{3+} signal can be spotted for the 2.5 uc GAO/STO sample. Note that part of the Ti^{3+} spectral weight may stem from localized Ti $3d$ charge carriers, trapped by oxygen vacancies [12]. The results of the quantitative analysis are summarized in Table II. While the two-dimensional charge carrier concentration $n_{2D} = p d_{2DES}/a^3$ is determined with good accuracy, only approximate parameter ranges can be appointed to the spatial extent d_{2DES} of the 2DES and the fraction p of Ti^{3+} ions. For a detailed discussion of the fit accuracy and error sources, see Supplemental Material.

The obtained charge carrier concentrations are higher than those determined similarly for LAO/STO heterostructures by one order of magnitude [12]. The resulting spatial expansion of the 2DES in the range of 5–20 Å is in agreement with the spatial expansion of the band bending d, which has been determined to be of the order of 15 Å. The formation of the 2DES inside the potential trough, formed by the band bending, is thus corroborated.

IV. DISCUSSION

The band arrangement at the heterointerface between a heteroepitaxial GAO film and a STO substrate as derived from HAXPES measurements is summarized in Fig. 9. The valence and conduction bands in STO are found to bend in vicinity of the interface. The maximum depth ΔE_{bb} of the band bending amounts to approximately 600 meV and extends by 3–5 unit cells into the substrate. At variance with the simple electronic reconstruction picture, no potential gradient is found inside the GAO overlayer. The relative band offset ΔE_{VB} between the flat GAO and the STO bulk band is ≈600 meV, about the same size as ΔE_{bb}, meaning that the bands are aligned at the interface. Published values for the band gap of STO show a rather large spread [41,42]. The indirect and direct band gaps of STO, as measured by ellipsometry are 3.25 eV and 3.75 eV, respectively [42]. It has been pointed out, that, for PES, a better measure for the band gap is determined from the onset of interband excitation in photoelectron energy
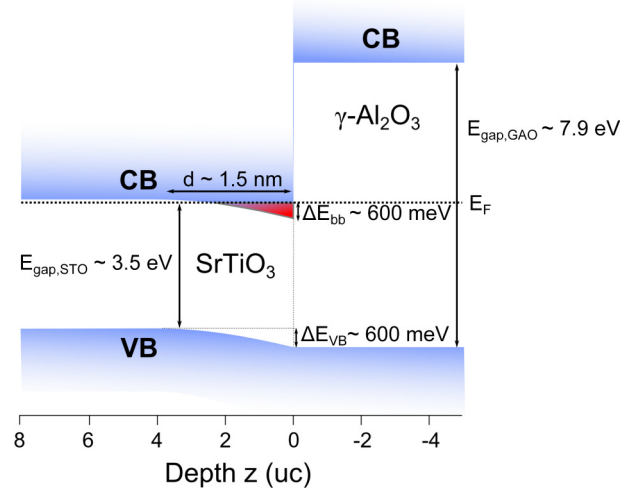

FIG. 9. (Color online) Band arrangement at the spinel/perovskite γ-Al$_2$O$_3$/SrTiO$_3$ heterointerface as inferred from HAXPES measurements. A significant bending of the conduction band below the chemical potential is found at the interface, forming a potential trough, which hosts the 2DES. The spatial expansion of approximately 15 Å of the 2DES is found to be in excellent agreement with the spatial depth of the potential trough. A valence band offset of approximately 600 meV is found, corresponding to aligned valence bands at the interface. The interface is of type I.

loss spectra from core level XPS, which yields (3.5 ± 0.1) eV [24]. Accordingly, the CBM of STO is found to be almost degenerate with the Fermi level in the bulk and bends below the chemical potential near the interface. Furthermore, due to its large band gap (≈ 7.9 eV) [20], the CBM of GAO is above that of STO. Accordingly, in contrast to LAO/STO [15,28,30,40], the heterointerface between GAO and STO is found to be of type I.

The apparent absence of any potential gradient in the GAO film is at variance with the polar-catastrophe scenario, which predicts a potential buildup in the stoichiometric polar overlayer owing to the polar discontinuity at the heterointerface [1,2]. Similar findings have been reported for LAO/STO heterostructures [23,29,30,43]. Different scenarios have been introduced to account for these observations, of which photoinduced carriers, oxygen vacancies, and antisite defects will be discussed in the following.

It is well known that light-induced photocarriers with lifetimes of several hours strongly affect the electrical conductivity in LAO/STO heterostructures [44]. It thus stands to reason that similar effects may occur in the related GAO/STO heterostructure. During HAXPES high-energy electron-hole pair excitations are created as side effects of photoelectron emission. After a rapid thermalization into the conduction and valence band, electrons and holes may get spatially separated due to the polar field and accumulate at the interface and the LAO surface, respectively. The resulting out-of-equilibrium state may fully compensate the intrinsic potential gradient. Although no indications for this scenario could be found in case of LAO/STO [30] it cannot ultimately be ruled out here.

Alternative explanations for the flat-band behavior in LAO/STO have been proposed by theoretical studies, which

consider a nonstoichiometric structure of overlayer and substrate. Several results point towards the formation of oxygen vacancies at the LAO surface, which become energetically favorable beyond a critical thickness [29,31,45–47]. Two electrons per (positively charged) oxygen vacancy remain, which can be transferred to the interface and counteract the polar field.

While the formation of oxygen vacancies offers an explanation for the apparent absence of a potential gradient above the critical overlayer thickness, the insignificant polar field in LAO films below the critical overlayer thickness is not accounted for [23]. Recently, a comprehensive mechanism based on the thermodynamically triggered formation of defects and antisite defects has been proposed [48]. While the origin of the 2DES at the *n*-type LAO/STO interface is also attributed to the formation of oxygen vacancies at the surface of LAO, the compensated potential below the critical LAO thickness is ascribed to Al-Ti antisite defects, which are furthermore held responsible for the formation of local magnetic moments and hence magnetism above the critical thickness [49–51]. In this picture, the emerging design principle for materials forming a 2DES comprises a polar discontinuity and the existence of donor defects with sufficiently low enthalpy of formation as well as a donor level higher in energy than the STO CBM, which may likely be met by GAO. A thorough theoretical investigation is needed to verify these assumptions and to draw further conclusions on this material.

The existence of oxygen vacancies at the STO side of the interface has been discussed as charge reservoir for the conducting interface in LAO/STO [3]. While such defects can contribute to the interfacial conductivity, an intrinsic carrier density of $1 \times 10^{13} - 3 \times 10^{13}$ charges/cm^2 remains after annealing at $600\,^\circ$C in oxygen atmosphere, thereby healing out all oxygen vacancies [52]. In GAO/STO, however, annealing in oxygen removes the conductivity at even lower temperatures (200–300 $^\circ$C), thus suggesting an important role of oxygen vacancies in STO for this system [13]. For this reason, emission angle-dependent O 1*s* core level spectra were measured for all heterostructures and bulk references of GAO and STO (see Supplemental Material). However, oxygen vacancies do not cause a direct spectroscopic signature in the oxygen core levels, which impedes a qualitative analysis. A quantitative analysis based on the lack of emitting oxygen atoms in the crystal structure is not possible, mainly due to the appearance of O 1*s* spectral weight caused by surface contaminants.

The O 2*p*-derived valence band structure has been thoroughly analyzed in Sec. III C and neither exhibits any spectral features traceable to oxygen vacancies. The direct observation of Ti 3*d* valence electrons due to oxygen vacancies and/or itinerant electrons forming the 2DES is impeded by the small photoionization cross section for HAXPES [53]. The role of oxygen defects and their relation to the appearance of a critical thickness in GAO/STO heterostructures remains to be further investigated.

V. SUMMARY

We have presented a detailed study of the band arrangement in GAO/STO heterostructures by using hard x-ray photoelectron spectroscopy. Our data reveal an apparent flat-band behavior in the GAO film, at variance with the expected potential gradient from the basic polar discontinuity scenario. Alternative explanations, considering the thermodynamically triggered formation of defects, are discussed with respect to the related LAO/STO heterostructure. An influence of photon-induced charge carriers leading to a nonequilibrium charge imbalance is discussed and cannot be ultimately excluded. Furthermore, we report a band bending inside the STO substrate, leading to the formation of a potential trough below the chemical potential with a depth of approximately 600 meV and a spatial expansion of roughly 3–5 unit cells of STO. The relative valence band offset at the interface is consistently determined to ≈600 meV by two independent methods, corresponding to aligned bands at the interface. In particular, and in contrast to LAO/STO, the GAO/STO interface is of type I. Finally, the spatial confinement of the 2DES is derived from the chemically shifted Ti^{3+} 2*p* photoemission signal caused by interfacial Ti 3*d* electrons. The resulting confinement to only a few unit cells STO is in excellent agreement with the obtained potential trough dimensions.

[1] A. Ohtomo and H. Y. Hwang, Nature (London) **427**, 423 (2004).

[2] S. Thiel, G. Hammerl, A. Schmehl, C. W. Schneider, and J. Mannhart, Science **313**, 1942 (2006).

[3] A. Brinkman, M. Huijben, M. van Zalk, J. Huijben, U. Zeitler, J. C. Maan, W. G. van der Wiel, G. Rijnders, D. H. A. Blank, and H. Hilgenkamp, Nat. Mater. **6**, 493 (2007).

[4] P. R. Willmott, S. A. Pauli, R. Herger, C. M. Schlepütz, D. Martoccia, B. D. Patterson, B. Delley, R. Clarke, D. Kumah, C. Cionca, and Y. Yacoby, Phys. Rev. Lett. **99**, 155502 (2007).

[5] S. A. Chambers, M. H. Engelhard, V. Shutthanandan, Z. Zhu, T. C. Droubay, L. Qiao, P. V. Sushko, T. Feng, H. D. Lee, T. Gustafsson, E. Garfunkel, A. B. Shah, J. M. Zuo, and Q. M. Ramasse, Surf. Sci. Rep. **65**, 317 (2010).

[6] N. Nakagawa, H. Y. Hwang, and D. A. Muller, Nat. Mater. **5**, 204 (2006).

[7] Y. Li and J. Yu, J. Appl. Phys. **108**, 013701 (2010).

[8] J. Lee and A. A. Demkov, Phys. Rev. B **78**, 193104 (2008).

[9] R. Pentcheva and W. E. Pickett, Phys. Rev. B **78**, 205106 (2008).

[10] K. Janicka, J. P. Velev, and E. Y. Tsymbal, Phys. Rev. Lett. **102**, 106803 (2009).

[11] M. Basletic, J.-L. Maurice, C. Carrétéro, G. Herranz, O. Copie, M. Bibes, É. Jacquet, K. Bouzehouane, S. Fusil, and A. Barthélémy, Nat. Mater. **7**, 621 (2008).

[12] M. Sing, G. Berner, K. Goß, A. Müller, A. Ruff, A. Wetscherek, S. Thiel, J. Mannhart, S. A. Pauli, C. W. Schneider, P. R. Willmott, M. Gorgoi, F. Schäfers, and R. Claessen, Phys. Rev. Lett. **102**, 176805 (2009).

[13] Y. Z. Chen, N. Bovet, F. Trier, D. V. Christensen, F. M. Qu, N. H. Andersen, T. Kasama, W. Zhang, R. Giraud, J. Dufouleur, T. S. Jespersen, J. R. Sun, A. Smith, J. Nygård, L. Lu, B. Büchner, B. G. Shen, S. Linderoth, and N. Pryds, Nat. Commun. **4**, 1371 (2013).

[14] Y. Z. Chen, N. Bovet, T. Kasama, W. W. Gao, S. Yazdi, C. Ma, N. Pryds, and S. Linderoth, Adv. Mater. **26**, 1462 (2013).

[15] S. A. Chambers, L. Qiao, T. C. Droubay, T. C. Kaspar, B. W. Arey, and P. V. Sushko, Phys. Rev. Lett. **107**, 206802 (2011).

[16] F. Schäfers, M. Mertin, and M. Gorgoi, Rev. Sci. Instrum. **78**, 123102 (2007).

[17] M. Gorgoi, S. Svensson, F. Schäfers, G. Öhrwall, M. Mertin, P. Bressler, O. Karis, H. Siegbahn, A. Sandell, H. Rensmo, W. Doherty, C. Jung, W. Braun, and W. Eberhardt, Nucl. Instrum. Methods Phys. Res., Sect. A **601**, 48 (2009).

[18] J. M. McHale, A. Auroux, A. J. Perrotta, and A. Navrotsky, Science **277**, 788 (1997).

[19] P. W. Tasker, J. Phys. C: Solid State Phys. **12**, 4977 (1979).

[20] B. Ealet, M. H. Elyakhloufi, E. Gillet, and M. Ricci, Thin Solid Films **250**, 92 (1994).

[21] R. S. Zhou and R. L. Snyder, Acta Crystallog. B: Struct. Sci. **47**, 617 (1991).

[22] S.-D. Mo, Y.-N. Xu, and W.-Y. Ching, J. Am. Ceram. Soc. **80**, 1193 (1997).

[23] Y. Segal, J. H. Ngai, J. W. Reiner, F. J. Walker, and C. H. Ahn, Phys. Rev. B **80**, 241107 (2009).

[24] S. A. Chambers, T. Droubay, T. C. Kaspar, M. Gutowski, and M. van Schilfgaarde, Surf. Sci. **554**, 81 (2004).

[25] J. J. Yeh and I. Lindau, At. Data Nucl. Data Tables **32**, 1 (1985).

[26] M. B. Trzhaskovskaya, V. I. Nefedov, and V. G. Yarzhemsky, At. Data Nucl. Data Tables **82**, 257 (2002).

[27] M. Takizawa, S. Tsuda, T. Susaki, H. Y. Hwang, and A. Fujimori, Phys. Rev. B **84**, 245124 (2011).

[28] G. Drera, G. Salvinelli, A. Brinkman, M. Huijben, G. Koster, H. Hilgenkamp, G. Rijnders, D. Visentin, and L. Sangaletti, Phys. Rev. B **87**, 075435 (2013).

[29] E. Slooten, Z. Zhong, H. J. A. Molegraaf, P. D. Eerkes, S. de Jong, F. Massee, E. van Heumen, M. K. Kruize, S. Wenderich, J. E. Kleibeuker, M. Gorgoi, H. Hilgenkamp, A. Brinkman, M. Huijben, G. Rijnders, D. H. A. Blank, G. Koster, P. J. Kelly, and M. S. Golden, Phys. Rev. B **87**, 085128 (2013).

[30] G. Berner, A. Müller, F. Pfaff, J. Walde, C. Richter, J. Mannhart, S. Thiess, A. Gloskovskii, W. Drube, M. Sing, and R. Claessen, Phys. Rev. B **88**, 115111 (2013).

[31] Y. Li, S. N. Phattalung, S. Limpijumnong, J. Kim, and J. Yu, Phys. Rev. B **84**, 245307 (2011).

[32] M. Salluzzo, J. C. Cezar, N. B. Brookes, V. Bisogni, G. M. De Luca, C. Richter, S. Thiel, J. Mannhart, M. Huijben, A. Brinkman, G. Rijnders, and G. Ghiringhelli, Phys. Rev. Lett. **102**, 166804 (2009).

[33] S. Kohiki, M. Arai, H. Yoshikawa, S. Fukushima, M. Oku, and Y. Waseda, Phys. Rev. B **62**, 7964 (2000).

[34] See Supplemental Material at http://link.aps.org/supplemental/10.1103/PhysRevB.91.165118 for details on the intrinsic spectra.

[35] B. L. Henke, E. M. Gullikson, and J. C. Davis, At. Data Nucl. Data Tables **54**, 181 (1993).

[36] S. Tanuma, T. Shiratori, T. Kimura, K. Goto, S. Ichimura, and C. J. Powell, Surf. Interface Anal. **37**, 833 (2005).

[37] S. A. Chambers, T. Droubay, T. C. Kaspar, and M. Gutowski, J. Vac. Sci. Technol., B: Microelectron. Process. Phenom. **22**, 2205 (2004).

[38] E. A. Kraut, R. W. Grant, J. R. Waldrop, and S. P. Kowalczyk, Phys. Rev. Lett. **44**, 1620 (1980).

[39] E. A. Kraut, R. W. Grant, J. R. Waldrop, and S. P. Kowalczyk, Phys. Rev. B **28**, 1965 (1983).

[40] L. Qiao, T. C. Droubay, T. C. Kaspar, P. V. Sushko, and S. A. Chambers, Surf. Sci. **605**, 1381 (2011).

[41] M. I. Cohen and R. F. Blunt, Phys. Rev. **168**, 929 (1968).

[42] K. v. Benthem, C. Elsässer, and R. H. French, J. Appl. Phys. **90**, 6156 (2001).

[43] B.-C. Huang, Y.-P. Chiu, P.-C. Huang, W.-C. Wang, V. T. Tra, J.-C. Yang, Q. He, J.-Y. Lin, C.-S. Chang, and Y.-H. Chu, Phys. Rev. Lett. **109**, 246807 (2012).

[44] M. Huijben, G. Rijnders, D. H. A. Blank, S. Bals, S. V. Aert, J. Verbeeck, G. V. Tendeloo, A. Brinkman, and H. Hilgenkamp, Nat. Mater. **5**, 556 (2006).

[45] Z. Zhong, P. X. Xu, and P. J. Kelly, Phys. Rev. B **82**, 165127 (2010).

[46] N. C. Bristowe, P. B. Littlewood, and E. Artacho, Phys. Rev. B **83**, 205405 (2011).

[47] N. Pavlenko, T. Kopp, E. Y. Tsymbal, J. Mannhart, and G. A. Sawatzky, Phys. Rev. B **86**, 064431 (2012).

[48] L. Yu and A. Zunger, Nat. Commun. **5**, 5118 (2014).

[49] L. Li, C. Richter, J. Mannhart, and R. C. Ashoori, Nat. Phys. **7**, 762 (2011).

[50] J. A. Bert, B. Kalisky, C. Bell, M. Kim, Y. Hikita, H. Y. Hwang, and K. A. Moler, Nat. Phys. **7**, 767 (2011).

[51] B. Kalisky, J. A. Bert, B. B. Klopfer, C. Bell, H. K. Sato, M. Hosoda, Y. Hikita, H. Y. Hwang, and K. A. Moler, Nat. Commun. **3**, 922 (2012).

[52] M. P. Warusawithana, C. Richter, J. A. Mundy, P. Roy, J. Ludwig, S. Paetel, T. Heeg, A. A. Pawlicki, L. F. Kourkoutis, M. Zheng, M. Lee, B. Mulcahy, W. Zander, Y. Zhu, J. Schubert, J. N. Eckstein, D. A. Muller, C. S. Hellberg, J. Mannhart, and D. G. Schlom, Nat. Commun. **4**, 2351 (2013).

[53] G. Berner, M. Sing, H. Fujiwara, A. Yasui, Y. Saitoh, A. Yamasaki, Y. Nishitani, A. Sekiyama, N. Pavlenko, T. Kopp, C. Richter, J. Mannhart, S. Suga, and R. Claessen, Phys. Rev. Lett. **110**, 247601 (2013).